



This is a repository copy of *Planform Effects for Low-Reynolds-Number Thin Wings with Positive and Reflex Cambers*.

White Rose Research Online URL for this paper:
<http://eprints.whiterose.ac.uk/130144/>

Version: Accepted Version

Article:

Chen, Z.J. and Qin, N. orcid.org/0000-0002-6437-9027 (2013) Planform Effects for Low-Reynolds-Number Thin Wings with Positive and Reflex Cambers. *Journal of Aircraft*, 50 (3). pp. 952-964. ISSN 0021-8669

<https://doi.org/10.2514/1.C032102>

Reuse

Items deposited in White Rose Research Online are protected by copyright, with all rights reserved unless indicated otherwise. They may be downloaded and/or printed for private study, or other acts as permitted by national copyright laws. The publisher or other rights holders may allow further reproduction and re-use of the full text version. This is indicated by the licence information on the White Rose Research Online record for the item.

Takedown

If you consider content in White Rose Research Online to be in breach of UK law, please notify us by emailing eprints@whiterose.ac.uk including the URL of the record and the reason for the withdrawal request.



eprints@whiterose.ac.uk
<https://eprints.whiterose.ac.uk/>

Planform Effects for Low-Reynolds-Number Thin Wings with Positive and Reflex Cambers

Z. J. Chen* and N. Qin†

University of Sheffield, Sheffield, England S1 3JD, United Kingdom

DOI: 10.2514/1.C032102

To understand the planform effects on low-Reynolds-number aerodynamic characteristics for micro air vehicles, various cambered thin plate wings were studied by numerical simulations based on Reynolds-averaged Navier–Stokes solutions with transition modeling. Six wing planforms, with the same wing aspect ratio and area, a positive camber at the quarter chord location, and a reflex camber near the trailing edge for longitudinal stability were selected for the study. They include a rectangular wing, four tapered wings with the same taper ratio but different leading-edge sweeps, a Zimmerman wing, and an inverse-Zimmerman wing. For validation with available wind-tunnel experimental data, an investigation of a circular wing planform with a similarly cambered profile is also presented. The results show that the Zimmerman wing planform gives the best lift-to-drag ratio at the design condition, whereas the tapered wing with higher leading-edge sweep produces higher maximum lift. Flow separation and vortical flow structures on the upper wing surface are presented to gain insight into the different aerodynamic characteristics for the different planforms.

Nomenclature

| | |
|-----------------|--|
| AR | = aspect ratio |
| b | = wing span, m |
| \bar{c} | = mean chord, m |
| C_D | = three-dimensional drag coefficient |
| C_L | = three-dimensional lift coefficient |
| $C_{L,max}$ | = maximum lift coefficient |
| $C_L/C_{D,max}$ | = maximum lift-to-drag ratio |
| C_M | = pitching moment coefficient |
| C_r | = wing root chord, m |
| C_t | = wingtip chord, m |
| D | = drag force, N |
| d_1 | = maximum positive camber location, m |
| d_2 | = maximum reflex camber location, m |
| h_1 | = maximum positive camber height, m |
| h_2 | = maximum reflex camber height, m |
| inZ | = inverse-Zimmerman wing |
| L | = lift force, N |
| Re | = Reynolds number based on chord |
| S | = wing area, m ² |
| t | = wing thickness, m |
| t/c | = thickness ratio |
| T_i | = turbulence intensity level |
| T_r | = taper ratio, C_t/C_r |
| U_∞ | = freestream velocity, m/s |
| x/c | = nondimensional chordwise location |
| X_{cg} | = distance between wing leading edge and center of gravity, m |
| X_{ac} | = distance between wing leading edge and aerodynamic center, m |
| Zim | = Zimmerman wing |
| z/b | = nondimensional spanwise location |
| α | = incidence/angle of attack, deg |

| | |
|-----------|---------------------------------|
| γ | = intermittency |
| Λ | = leading-edge sweep angle, deg |

I. Introduction

KEY geometric parameters in micro air vehicle design (MAV) include the airfoil section (thickness, camber, etc.) and wing planform (aspect ratio, shape, etc.), as mentioned by Pines and Bohorquez [1]. Along with the effects of these geometric parameters, operating at a low-Reynolds-number range with strong viscous effects, flow separation and reattachment, vortices, and boundary-layer transitions can all significantly affect the wing aerodynamics [2,3].

Because of the low-Reynolds-number effects and practical issues, thin airfoil profiles are preferred for MAV designs. Pelletier and Mueller [4] studied different thin/cambered airfoils for a rectangular wing planform with Re ranging from 60,000 to 200,000. The wind-tunnel results showed that a 4% cambered wing (without reflex camber) offers better aerodynamic characteristics than a flat-plate wing for given Reynolds number and aspect ratio. The flow on the cambered wing remained attached for a higher incidence than that for the flat-plate wing. These thin plate wings did not experience abrupt stall, and the lift force often reached a plateau and then remained relatively constant. However, there were no particular reasons provided to explain this phenomenon. Swanson and Isaac [5] studied planform and camber effects on low-Reynolds-number aerodynamics computationally. An extremely low Reynolds number of 500 was investigated, and they showed that the tip vortex is the dominant flow, and it forms the highly three-dimensional (3-D) low-velocity region at high incidences. Tezuka et al. [6] also investigated the surface flow structure on a 4% cambered plate at a Reynolds number of 93,000. The laminar separation bubble was clearly shown by the oil flow technique on the upper wing surface, and the pressure distribution with a plateau following the suction peak near the leading edge also appeared.

The reflex camber is another issue for a MAV to perform in a longitudinal stable flight as a flying wing. The combined positive and reflex camber effects on MAV aerodynamic characteristics were studied by Reid and Kozak [7] and Null and Shkarayev [8] separately. Reid and Kozak focused on a rectangular wing ($AR = 2$) planform with a positive camber varied from 1 to 9% c located at 25% c and a fixed reflex camber of 1% c located at 85% c . The surface oil flow visualization was taken in the investigation. The laminar separation bubble was found to be a key phenomenon, depending on the camber,

Received 10 September 2012; revision received 6 November 2012; accepted for publication 19 November 2012; published online XX epubMonth XXXX. Copyright © 2012 by the American Institute of Aeronautics and Astronautics, Inc. All rights reserved. Copies of this paper may be made for personal or internal use, on condition that the copier pay the \$10.00 per-copy fee to the Copyright Clearance Center, Inc., 222 Rosewood Drive, Danvers, MA 01923; include the code 1542-3868/YY and \$10.00 in correspondence with the CCC.

*Ph.D. Research Student, Department of Mechanical Engineering.

†Professor of Aerodynamics, Department of Mechanical Engineering; n.qin@sheffield.ac.uk. Associate Fellow AIAA (Corresponding Author).

Reynolds number, and incidence. At a given incidence and Reynolds number, the separation point moves downstream as the camber increases, and the flow fails to reattach after separation as the camber is above 6%. The force measurement showed that the $(C_L/C_D)_{\max}$ depends strongly on both the positive camber at 25% c and the Reynolds number. Unfortunately, there were no further studies on the influence of the reflex camber and its location. Null and Shkarayev [8] studied a circular wing planform with various cambers (both positive and reflex cambers) at a Re of 50,000; 75,000; and 100,000. The positive cambers varied from 3 to 12% c . For the high-speed flight ($Re = 100,000$), the 3% camber gave the best $((C_L/C_D)_{\max})$ value of 6.5, and for the low-speed flight, 6 and 9% camber offer better $(C_L/C_D)_{\max}$ values.

On the effect of wing planforms at low Re , however, most work focuses on the flat-plate geometries without a camber. Torres and Mueller [9] investigated flat-plate wing planforms with different aspect ratios at low Reynolds numbers. The results indicated that, for $AR > 1.5$, the elliptical planform is more aerodynamically efficient than the other planforms studied. Beside this, as the aspect ratio increased, the stall angle occurred earlier, and a relatively constant lift appeared after the stall angle as the incidence increased further, but the lift slope $C_{L\alpha}$ became more linear than lower-aspect-ratio wings. More recently, Okamoto and Azuma [10] studied a series of flat-plate wing planforms at an even lower Reynolds number of 10,000. A strong planform effect was found for low-aspect-ratio MAV wings. Zuo and Wang [11] also investigated experimentally flat-plate wing planforms with different leading-edge (LE) sweep angles. The wing has a low aspect ratio at a relatively higher Reynolds number of 273,000. From surface oil flow visualization and force measurements, it was found that, for a sweep angle $\Lambda < 35$ deg, C_L drops abruptly after stall, but C_L decreases more gradually after stall as the sweep angle increases beyond 50 deg. The large vortex flow on the upper wing surface varied with the incidence, and the detachment of the vortices was associated with the abrupt drop of C_L . The sweep angle was found to alter the stall behavior significantly. Zhang et al. [12] performed a similar investigation on sweep angle/taper ratio effects at a Reynolds number of 342,000. 3-D leading-edge separation bubbles were observed at low incidences, varying with the sweep angles. They confirmed the sweep effect on the wing stall type and pointed out that the reason may be due to the different leading-edge vortex structures. An elliptical wing planform was also studied by Jian and Ke-Qin [13] both numerically and experimentally. They pointed out that at an incidence larger than 11 deg the flow becomes bilaterally asymmetric. It is mainly due to the tip vortices' destabilization. As the angle of attack increased to 33 deg, a large separated vortex stayed above the wing and formed a stationary vortex. Delta wings at low Reynolds numbers were also studied by several investigators, such as Ol and Gharib [14] and Wang and Zhang [15], etc. (i.e., investigated the leading-edge vortex structure at low Reynolds numbers).

From the literature, as far as the MAV planform study is concerned, investigation on planform effects has so far been limited to flat-plate wings. In the present work, various MAV planforms are investigated for thin cambered wings, with both positive and reflex cambers, at a low Reynolds number. The study is divided into the following three parts:

- 1) A validation case is performed, and results are compared with the experimental data.
- 2) The aerodynamic performance of camber plate wings of different planforms is simulated and analyzed, and the results are compared.
- 3) 3-D flow structures at both design and stall conditions are investigated and discussed.

II. Numerical Procedure

The flow around the MAV geometries is solved based on the incompressible Navier–Stokes equations coupled with a transition model using the FLUENT flow solver. A finite volume approach is employed to discretize the governing equations, which are solved with a pressure-based algorithm. The convection terms are

discretized with the second-order upwind scheme and the diffusion terms with the second-order central-difference scheme. Menter's [16] k - ω -Shear Stress Transport (SST) turbulence model is used to close the RANS equations. For clarity, the turbulence model with the transition model is shown here.

$$\frac{\partial \rho k}{\partial t} + \frac{\partial (\rho u_i k)}{\partial x_i} = \frac{\partial}{\partial x_j} \left(\left(\mu + \frac{\mu_t}{\sigma_k} \right) \frac{\partial k}{\partial x_j} \right) + \tilde{G}_k - Y_k + S_k \quad (1)$$

$$\frac{\partial \rho \omega}{\partial t} + \frac{\partial (\rho u_i \omega)}{\partial x_i} = \frac{\partial}{\partial x_j} \left(\left(\mu + \frac{\mu_t}{\sigma_\omega} \right) \frac{\partial \omega}{\partial x_j} \right) + G_\omega - Y_\omega + D_\omega + S_\omega \quad (2)$$

where $\mu_t = \frac{\rho k}{\omega} \frac{1}{\max\left[\frac{1}{L_0^*}, \frac{1}{L_0^*}, \frac{1}{L_0^*}\right]}$, $\alpha^* = \alpha_\infty^* \left(\frac{\alpha_0^* + Re_i/R_k}{1 + Re_i/R_k} \right)$, $\alpha_0^* = \frac{0.073}{3}$, $S = \sqrt{2S_{ij}S_{ij}}$, $\sigma_k = \frac{1}{F_1/\sigma_{k,1} + (1-F_1)/\sigma_{k,2}}$, $\sigma_\omega = \frac{1}{F_1/\sigma_{\omega,1} + (1-F_1)/\sigma_{\omega,2}}$, \tilde{G}_k represents the generation of turbulence kinetic energy due to mean velocity gradients, G_ω represents the generation of ω , Y_k and Y_ω represent the dissipation of k and ω due to turbulence, D_ω represents the cross-diffusion term, and S_k , S_ω are user-defined sources terms.

The production of kinetic energy, k , is

$$\tilde{G}_k = \min \left(-\overline{\rho u_i' u_j'} \frac{\partial u_j}{\partial x_i}, 10\rho\beta^* k \omega \right)$$

and the production of ω is

$$G_\omega = \frac{\alpha}{\nu_t} \left(-\overline{\rho u_i' u_j'} \frac{\partial u_j}{\partial x_i} \right)$$

The dissipation of k is given by

$$Y_k = \rho\beta^* f_{\beta^*} k \omega, \quad f_{\beta^*} = \begin{cases} 1 & x_k \leq 0 \\ \frac{1}{1+400x_k^2} & x_k > 0 \end{cases}$$

$$x_k = \frac{1}{\omega^3} \frac{\partial k}{\partial x_j} \frac{\partial \omega}{\partial x_j}, \quad \beta^* = \beta_i^* [1 + \zeta^* F(M_t)]$$

$$\beta_i^* = \beta_\infty^* \left[\frac{\frac{4}{14} + \left(\frac{Re_i}{R_\beta}\right)^4}{1 + \left(\frac{Re_i}{R_\beta}\right)^4} \right] \quad \text{and} \quad \zeta^* = 1.5, \quad R_\beta = 8,$$

$$\beta_\infty^* = 0.09$$

and the dissipation of ω is given by

$$Y_\omega = \rho\beta f_\beta \omega^2, \quad f_\beta = \frac{1 + 70x_\omega}{1 + 80x_\omega}, \quad x_\omega = \left| \frac{\Omega_{ij}\Omega_{jk}S_{ki}}{(\beta_\infty^* \omega)^3} \right|,$$

$$\Omega_{ij} = \frac{1}{2} \left(\frac{\partial u_i}{\partial x_j} - \frac{\partial u_j}{\partial x_i} \right), \quad \text{and} \quad \beta = \beta_i [1 - \frac{\beta_i^*}{\beta_i} \zeta^* F(M_t)]$$

The cross-diffusion term D_ω is given by

$$D_\omega = 2(1 - F_1)\rho\sigma_{\omega,2} \frac{1}{\omega} \frac{\partial k}{\partial x_j} \frac{\partial \omega}{\partial x_j}$$

The SST model coefficients are blended between the inner and outer zones given by the expression

$$\sigma = F_1\sigma_{k-e} + (1 - F_1)\sigma_{k-\omega}$$

The blending function F_1 is one at the wall and zero far away from the wall, thus activating the Wilcox [17] k - ω model in the near-wall region and the k - ω model for the outer zone. The blending function F_1 is given by

$$F_1 = \tan h(\Phi_1^4)$$

$$\Phi_1 = \min \left[\max \left(\frac{\sqrt{k}}{0.09\omega y}, \frac{500\mu}{\rho\omega y^2} \right), \frac{4Qk}{\sigma_{\omega,2} D_{\omega}^+ y^2} \right]$$

$$D_{\omega}^+ = \max \left[2\rho \frac{1}{\sigma_{\omega,2}} \frac{1}{\omega} \frac{\partial k}{\partial x_j} \frac{\partial \omega}{\partial x_j}, 10^{-10} \right]$$

where, y is the distance to the next surface, D_{ω}^+ is the positive portion of the cross-diffusion term, $\sigma_{k,1} = 1.176$, $\sigma_{\omega,1} = 2.0$, $\sigma_{k,2} = 1.0$, $\sigma_{\omega,2} = 1.168$, and $\alpha_1 = 0.31$.

An additional transport equation is used to trigger the transition locally, and the intermittency function γ [18] is coupled with the k - ω -SST turbulence model. The main requirements for this transition model are the local variables and gradients, as well as the wall distance. The intermittency equation is given as

$$\frac{\partial(\rho\gamma)}{\partial t} + \frac{\partial(\rho u_j \gamma)}{\partial x_j} = P_{\gamma 1} - E_{\gamma 1} + P_{\gamma 2} - E_{\gamma 2} + \frac{\partial}{\partial x_j} \left[\left(\mu + \frac{\mu_t}{\sigma_f} \right) \frac{\partial \gamma}{\partial x_j} \right] \quad (3)$$

The transition sources are $P_{\gamma 1} = F_{\text{length}} \rho S [\gamma F_{\text{onset}}]^{c_{a1}}$, and $E_{\gamma 1} = c_{e1} P_{\gamma 1} \gamma$.

The function F_{onset} is used to trigger the intermittency production, given by

$$F_{\text{onset}} = \max(F_{\text{onset},2} - F_{\text{onset},3}, 0)$$

where

$$F_{\text{onset},2} = \min[\max(F_{\text{onset},1}, F_{\text{onset},1}^4), 2.0],$$

$$F_{\text{onset},1} = \frac{Re_v}{2.193 Re_{\theta c}}$$

$$F_{\text{onset},3} = \max \left[1 - \left(\frac{R_T}{2.5} \right)^3, 0 \right]$$

The viscosity ratio $R_T = \frac{\rho k}{\mu \omega}$, the vorticity Reynolds number $Re_v = \frac{\rho v^2 \delta}{\mu}$, and $Re_{\theta c}$ is the critical Reynolds number for which the intermittency first occurs.

The relaminarization sources are $P_{\gamma 2} = c_{a2} \rho \Omega \gamma F_{\text{turb}}$, $E_{\gamma 2} = c_{e2} P_{\gamma 2} \gamma$, and $F_{\text{turb}} = \exp(-\frac{R_T}{4})^4$ with the constants $c_{e1} = 1.0$, $c_{a1} = 0.5$, $c_{e2} = 50$, $c_{a2} = 0.03$, and $\sigma_f = 1.0$.

The equation for the transition momentum thickness Reynolds number $\tilde{R}_{e\theta t}$ is given by

$$\frac{\partial(\rho \tilde{R}_{e\theta t})}{\partial t} + \frac{\partial(\rho u_j \tilde{R}_{e\theta t})}{\partial x_j} = P_{\theta t} + \frac{\partial}{\partial x_j} \left[\sigma_{\theta t} (\mu + \mu_t) \frac{\partial \tilde{R}_{e\theta t}}{\partial x_j} \right] \quad (4)$$

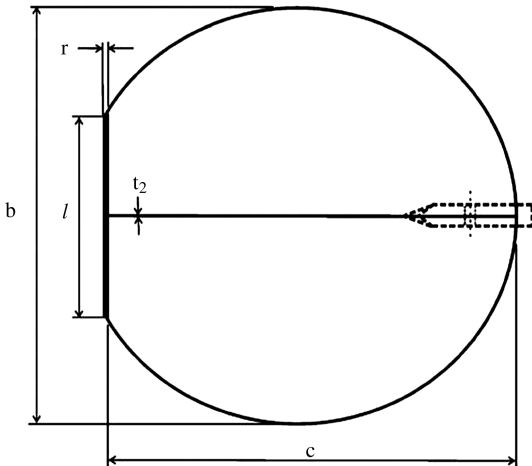


Fig. 1 MAV with a circular wing planform [8].

Table 1 Validation case parameters for the circular wing MAV

| Parameter | Value |
|--------------------------|---------------------------|
| Wing area, S | 0.0387 m ² |
| Chord length, c | 0.206 m |
| Positive camber | 0.0124 m |
| Reflex camber | 4.75 × 10 ⁻³ m |
| Wing thickness, t | 5.08 × 10 ⁻⁴ m |
| Positive camber location | 0.0495 m |
| Reflex camber location | 0.1794 m |
| Wing span, b | 0.2286 m |

The source terms are defined as the following:

$$P_{\theta t} = c_{\theta t} \frac{\rho}{t} (R_{e\theta t} - \tilde{R}_{e\theta t}) (1.0 - F_{\theta t})$$

$$t = \frac{500\mu}{\rho U^2}$$

where t is a time scale that is present for dimensional reasons. The blending function $F_{\theta t}$ is used to turn off the source term in the boundary layer and allow the transported scalar $\tilde{R}_{e\theta t}$ to diffuse in from the freestream. $F_{\theta t}$ is zero in the freestream and one in the boundary layer. It is defined as

$$F_{\theta t} = \min \left\{ \max \left[F_{\text{wake}} e^{-(y/\delta)^4}, 1.0 - \left(\frac{\gamma - 1/c_{e2}}{1.0 - 1/c_{e2}} \right)^2 \right], 1 \right\}$$

$$\theta_{BL} = \frac{\tilde{R}_{e\theta t} \mu}{\rho U} \quad \delta_{BL} = \frac{15}{2} \theta_{BL} \quad \text{and} \quad \delta = \frac{50 \Omega y}{U} \delta_{BL} \quad Re_{\omega} = \frac{\rho \omega y^2}{\mu}$$

$$F_{\text{wake}} = e^{-[Re_{\omega}/(1E+5)]^2}$$

The constants are $c_{\theta t} = 0.03$ and $\sigma_{\theta t} = 10.0$. The boundary condition for $\tilde{R}_{e\theta t}$ at a wall is zero flux, and it should be calculated from the empirical correlation based on the inlet turbulence intensity for the inlet boundary condition; more details can be seen in [18,19]. This model has been used by a number of researchers for low-Re transitional flows. For example, Benyahia [20] conducted a validation study for the model for low-Re number flows. According to the comparison between the numerical and experimental data, it was shown that this transition-SST model accurately predicts the location and extent of the laminar separation bubble. For proper behavior of the transition model, the $y+$ value for the first cell above the wall has to be on the order of one, as recommended by Menter et al. [18].

III. Details of the Computations

The following section is divided into two subsections: geometry description and computational setup, including both mesh topologies and boundary conditions.

A. Geometry Description

Figure 1 shows the geometry for the validation case, and the MAV model has a circular wing planform. This wing was investigated by Null and Shkarayev [8] experimentally. The flow conditions are a

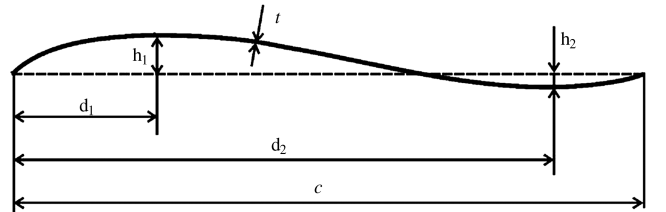


Fig. 2 Airfoil used in this study.

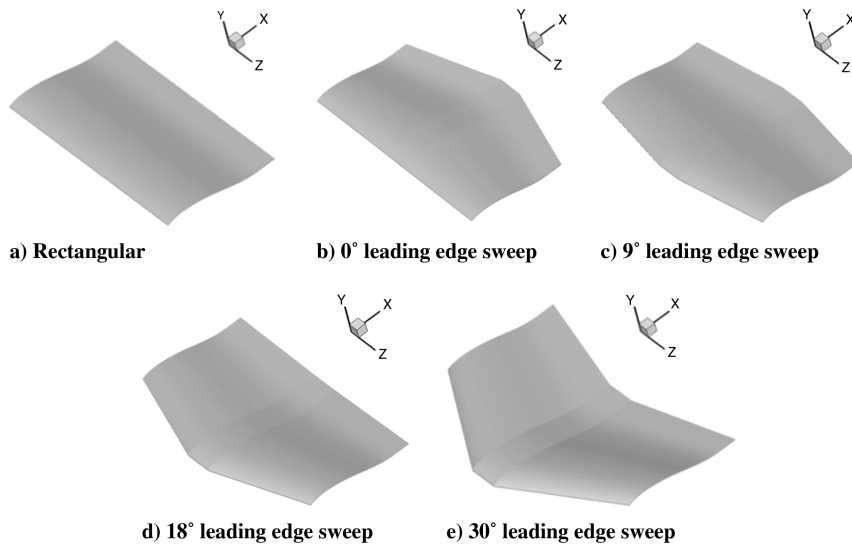


Fig. 3 Trapezoidal planform geometries.

freestream velocity of 10 m/s and an aerodynamic chord of 0.206 m, and this gives a Reynolds number of 100,000. The given experimental uncertainties are ± 0.07 N for lift, ± 0.06 N for drag, and ± 0.073 Nm for the pitching moment. The airfoil has a positive camber of $6\% \bar{c}$ and a reflex camber of $2.3\% \bar{c}$, located at $24\% \bar{c}$ and $87\% \bar{c}$, respectively. The model has a wing area of 0.0387 m² with a mean chord length of 206 mm and a thickness of 0.508 mm. All the parameters are listed in Table 1.

After validation, different planforms with a thickness of $0.9\% \bar{c}$ are investigated. The camber line shown in Fig. 2 [8] indicates the parameters in the camber line design. Based on previous studies [5–8], a positive camber of $5.8\% \bar{c}$ located at 25% of the mean chord and a reflex camber of $1\% \bar{c}$ located $86\% \bar{c}$ are chosen for all of the following planform studies. The reflex camber is introduced in the design for longitudinal stability for these flying wing configurations without the tail plane, although it also reduces the overall aerodynamic performance. The flow conditions are a freestream of 10 m/s and a mean aerodynamic chord of 0.2214 m, and this gives a Reynolds number of 150,000 (Table 2).

To study the cambered thin plate wings, four distinct geometries were selected, namely, rectangular, tapered wings with swept leading edges, Zimmerman, and inverse-Zimmerman, as shown in Figs. 3 and 4. The choice of these planforms are based on some current often-used MAV planform designs. For example, the Wasp MAV by AeroVironment [21] and UGMVAV from the University of Ghent [22] took a low-aspect-ratio tapered wing planform design. The micro tactical expendable (MITE) MAVs from the Naval Research Laboratory [23] and Hornet MAVs of AeroVironment [24] were based on a simple low-aspect-ratio rectangular design. Tapered wings with high-leading-edge sweep were adopted for the Zagi MAV [24], and Zimmerman planforms were used in the Dragonfly MAV by the University of Arizona [25], Florida MAVs [26], and the thrust-vectored MAV by the University of Sheffield [27]. No detailed comparison of the aerodynamic performance at low Reynolds numbers for these different planforms can be found in the literature, giving the reason for the present study.

Table 3 shows the specifications of the different MAV planforms, all having the same wing area of 0.0895 m², the same aspect ratio of 2.12, and a mean aerodynamic chord of 0.221 m. The tapered wings also have the same taper ratio of 0.44. The root chords are 0.25 m for all wings except for the rectangular wing.

B. Mesh and Boundary Conditions

In the simulations, fully structured meshes are generated by the ICEM mesh generation program, as shown in Fig. 5. All models have a circular leading edge and a sharp trailing edge. A structured C - H type mesh topology is chosen for the calculations, as shown in Fig. 5. The freestream Reynolds number based on the chord length is set to

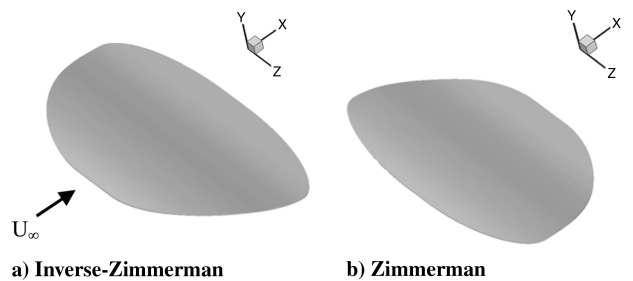


Fig. 4 a) Zimmerman and b) inverse-Zimmerman planform geometries.

100,000. A symmetric boundary condition is applied at the wing root plane. The no-slip wall boundary condition is enforced on the wing surface, and the far-field condition is set for the far-field boundary. To minimize the effect of the far-field boundary on the accuracy of the solutions near the geometry, the outer domains were placed at $12c$ in the upstream, upward, and downward directions; $15c$ for the downstream; and $10c$ in the span direction.

Table 2 Thin plate airfoil camber parameters

| Parameter | Value |
|---------------|----------|
| d_1/\bar{c} | 25% |
| d_2/\bar{c} | 86% |
| h_1/\bar{c} | 5.8% |
| h_2/\bar{c} | 1% |
| t/\bar{c} | 0.9% |
| \bar{c} | 0.2214 m |

Table 3 Wing planform specifications^{ab}

| Wing planform | C_r , m | C_t , m | Λ , deg | B, m |
|-------------------|-----------|-----------|-----------------|------|
| Rectangular | 0.221 | 0.221 | 0 | 0.4 |
| LE sweep 0 deg | 0.250 | 0.193 | 0 | 0.4 |
| LE sweep 9 deg | 0.250 | 0.193 | 9 | 0.4 |
| LE sweep 18 deg | 0.250 | 0.193 | 18 | 0.4 |
| LE sweep 30 deg | 0.250 | 0.193 | 30 | 0.4 |
| Inverse-Zimmerman | 0.250 | — | — | 0.44 |
| Zimmerman | 0.250 | — | — | 0.44 |

^a $C_{L,required}$ is the required lift coefficient for the design condition.

^bDesign condition $C_{L,required} = 0.35$.

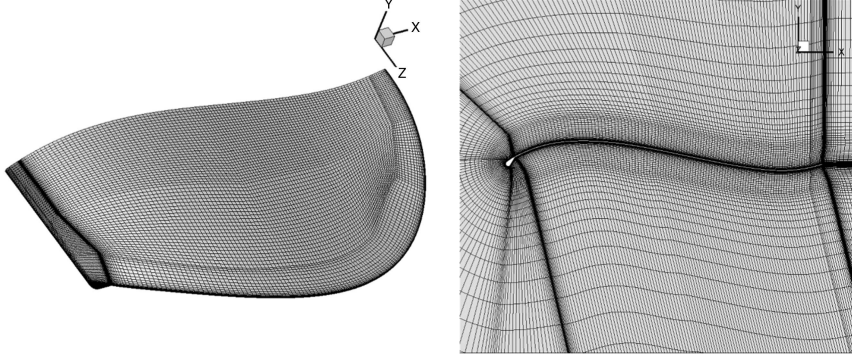


Fig. 5 Mesh topology for the validation case.

Table 4 Grid sensitivity analysis for $\alpha = 0$ and 10 deg

| Case | Size | α , deg | Grid size | C_L | C_D |
|------------|-----------------|----------------|---------------------------|------------------|------------------|
| 1 | 2×10^6 | 0 | $276 \times 55 \times 58$ | 0.108 | 0.047 |
| | | 10 | $276 \times 55 \times 58$ | 0.585 | 0.119 |
| 2 | 4×10^6 | 0 | $402 \times 70 \times 75$ | 0.106 | 0.047 |
| | | 10 | $402 \times 70 \times 75$ | 0.604 | 0.125 |
| 3 | 6×10^6 | 0 | $478 \times 90 \times 86$ | 0.109 | 0.052 |
| | | 10 | $478 \times 90 \times 86$ | 0.599 | 0.125 |
| Experiment | — | 0 | — | 0.097 ± 0.12 | 0.036 ± 0.05 |
| | | 10 | — | 0.639 ± 0.12 | 0.129 ± 0.05 |

C. Mesh Sensitivity Study and Validation with Experimental Data

Table 4 lists the results based on the grid sensitivity analysis for the circular wing at two incidences of 0 and 10 deg. From this mesh sensitivity study, mesh 2, the grid with $402 \times 70 \times 75$ points, is chosen for all computations reported later as it gives reasonably accurate results in the force coefficients. Figure 6 shows the aerodynamic coefficients versus the angle of attack, showing good agreement with the experiment data below 25 deg, and underpredictions are found in the stall region. For the resolution of the turbulent boundary layer, the y^+ value needs to be on the order of $O(1)$, which is satisfied as shown in Fig. 7.

IV. Results and Discussion

The Results and Discussion section (Sec. III) is organized into 1) a comparison of aerodynamic performance at the given design conditions for the different planforms, 2) a detailed study of the trapezoidal wings with different leading-edge sweep angles, and 3) a detailed study of the Zimmerman and inverse-Zimmerman wings.

A. Comparison at the Given Design Condition

The design conditions for testing the various planforms are based on the requirement for our flying MAV prototype with a design weight of 200 g, as shown in Fig. 8, with a thrust vector propeller cruising at 20 m/s and a Zimmerman wing planform. This MAV has been flight tested with the fuselage, the propeller in a tractor configuration, and a vertical stabilizer. Note that, in the current paper, only the wing itself is studied without the influence of the other components. Table 5 shows the aerodynamic efficiencies of the various planforms defined in the last section at the design lift condition of $C_L = 0.35$. The solution was run iteratively to satisfy the

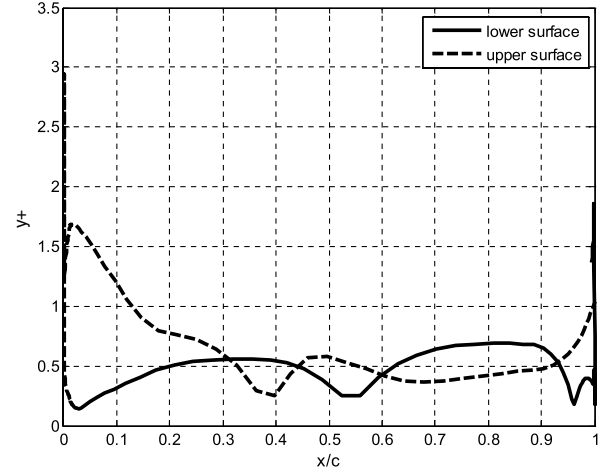


Fig. 7 y^+ value.

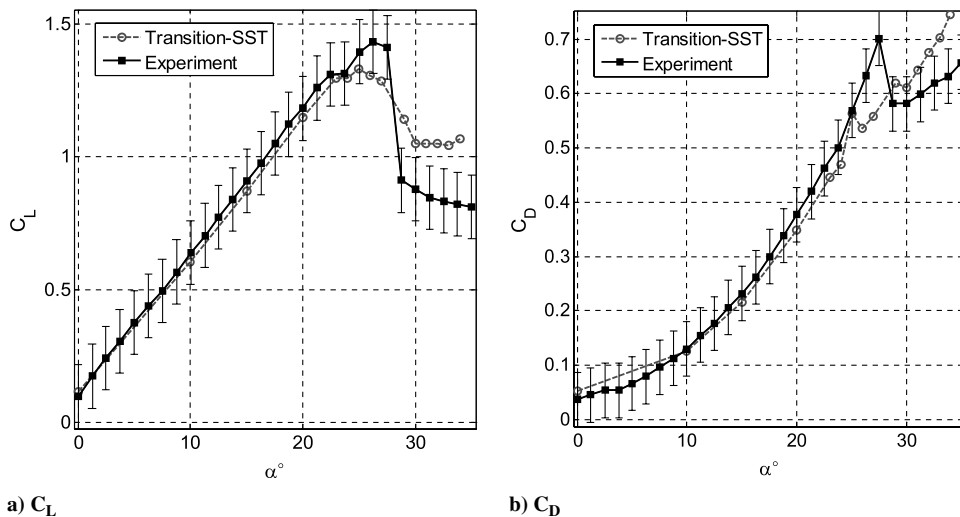


Fig. 6 Aerodynamic coefficients for mesh set $402 \times 70 \times 75$: a) C_L and b) C_D .

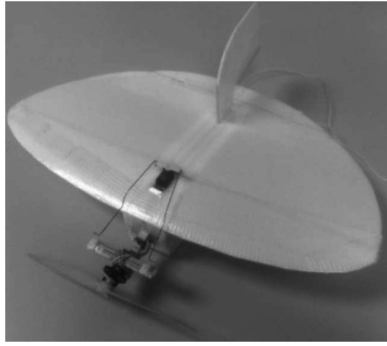


Fig. 8 MAV prototype.

design lift condition, and in the process, the required incidences for the different wings were found. As can be observed from the table, the design lift is achieved at relatively small incidences for this particular positive and reflex camber design.

All the tapered wings, with the same taper ratio of 0.44, have better aerodynamic performance than the rectangular wing. Among them, the one with the largest leading-edge sweep produces a significantly better lift-drag ratio. The inverse-Zimmerman wing is the poorest

Table 5 Aerodynamic coefficients at the design conditions

| Wing planform | $C_{D,dc}$ | $C_{M,dc}$ | $C_L/C_{L,dc}$ | α_{dc} , deg | Lift slope ^a |
|-------------------|------------|------------|----------------|---------------------|-------------------------|
| Rectangular | 0.0578 | 0.0682 | 6.052 | 1.43 | 0.0531 |
| Tapered 0 deg LE | 0.0567 | 0.0671 | 6.172 | 1.57 | 0.0531 |
| Tapered 9 deg LE | 0.0571 | 0.0669 | 6.134 | 1.59 | 0.0550 |
| Tapered 18 deg LE | 0.0568 | 0.0687 | 6.165 | 1.45 | 0.0535 |
| Tapered 30 deg LE | 0.0504 | 0.0652 | 6.944 | 1.69 | 0.0567 |
| Inverse-Zimmerman | 0.0626 | 0.0725 | 5.869 | 0.45 | 0.0573 |
| Zimmerman | 0.0468 | 0.0439 | 7.475 | -1.03 | 0.0567 |

$$^a a = \frac{\partial C_L}{\partial \alpha}$$

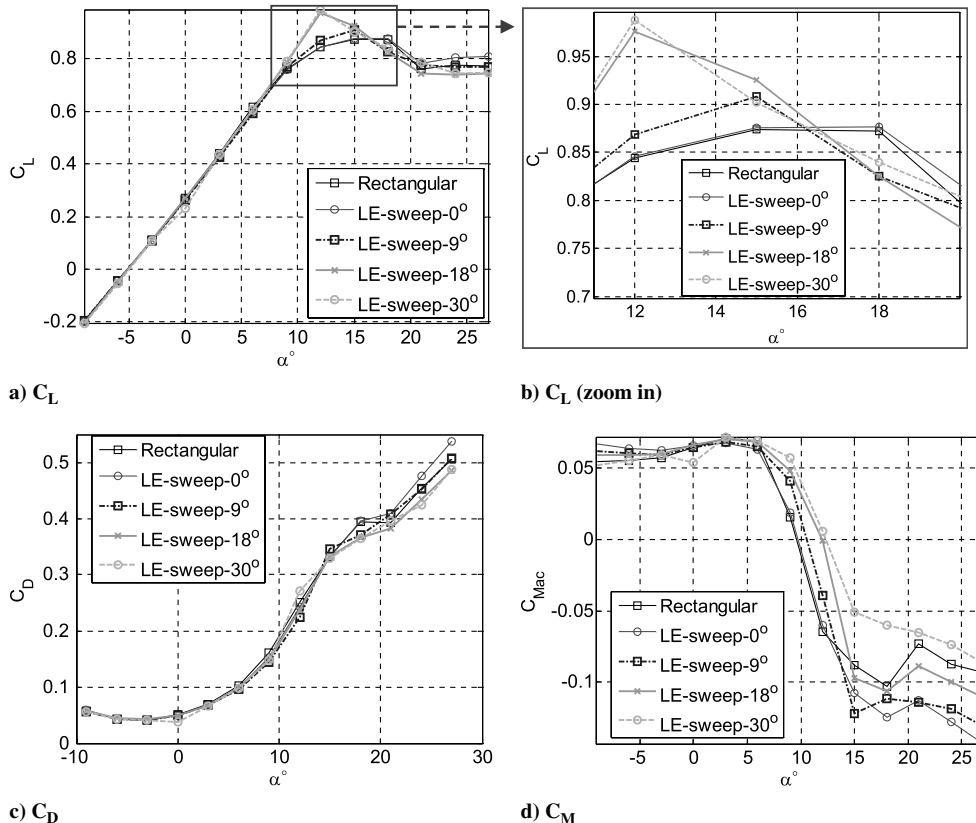


Fig. 9 Aerodynamic performance for isolated swept wing planforms.

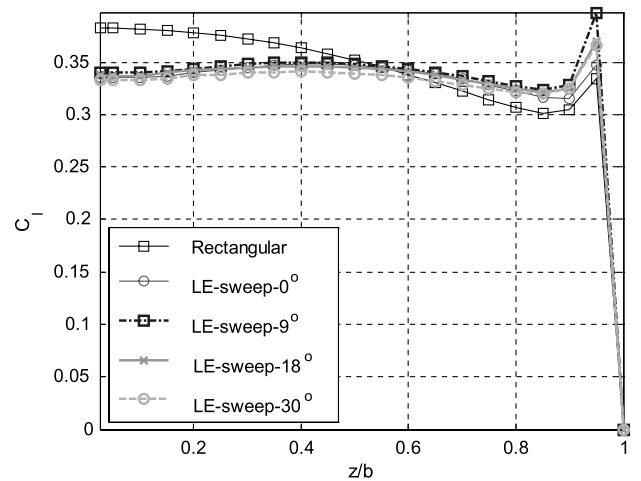


Fig. 10 Spanwise C_L distributions at the design condition.

among the candidates, whereas the Zimmerman wing gives the best aerodynamic performance at the design condition. A series of angles of attack from -6 to 27 deg are simulated every three degrees.

B. Tapered Wing with Different Leading-Edge Sweep

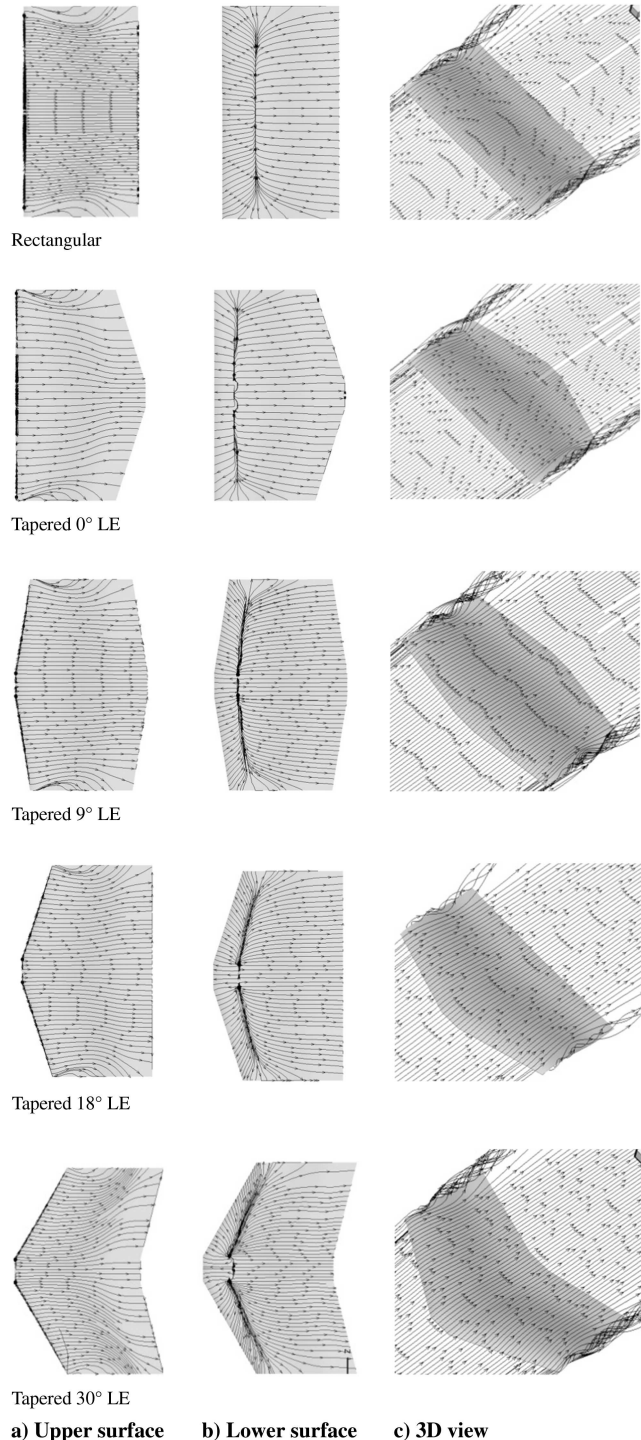
1. Aerodynamic Performance

The aerodynamic performance plots of the trapezoidal wings in Fig. 9a show that all wing planforms have the similar lift slope $C_{L\alpha}$ in the near-linear parts of the curves at low incidences, despite the differences in the aerodynamic performance shown in Table 5. A strong effect of leading-edge sweep is shown in Fig. 9b. The 18 and 30 deg sweep wings have the highest $C_{L,max}$ of 0.97–0.98 with a significant sudden drop of lift at stall. As the leading-edge sweep reduces, the stall behavior becomes more gradual with decreased $C_{L,max}$.

The sweep angle also has a noticeable influence on the pitching moment coefficient. The trapezoidal wings have a positive C_{ma} at incidences between -9 to 5 deg, implying longitudinal instability if the wings are used alone at low incidences. The two-dimensional spanwise lift distribution, C_l in Fig. 10, indicates that the tapered wings have a more constant C_l distribution along the wing span than the rectangular wing. They also show higher loading near the wingtips.

2. Surface and 3-D Streamlines

Figure 11 shows the surface streamlines for the trapezoidal wings at the design condition. Fully attached flow is observed on all the



a) Upper surface b) Lower surface c) 3-D view
Fig. 11 Stream patterns at the design condition: a) upper surface, b) lower surface, and c) 3-D view; flow from left.

upper wing surfaces, and leading-edge separation bubbles form on the lower surfaces for all shapes. All the trapezoidal wings show the wingtip effects on the surface streamline curvature. The spanwise flow strengthens as the leading-edge sweep increases. On the lower wing surface, variation of the leading-edge separation bubble is also observed, depending on the leading-edge sweep. There is a large difference in the laminar separation bubbles for the tapered wing with zero sweep and the rectangular wing.

The spanwise C_p distributions at different chordwise locations are shown in Fig. 12. The suction peaks are most prominent in the plots for the $25\%c$ location, indicating the wingtip vortex effect. The peak C_p value is similar to the Zimmerman wing case shown later.

C. Zimmerman vs Inverse-Zimmerman

URANS simulations are performed for both Zimmerman and inverse-Zimmerman wing planforms. The simulation was performed with various incidences from -6 to 27 deg, and the time step was set to be 4.428×10^{-4} s for both wing planform models. The time averaging for URANS was made based on the results of 300 time steps after the solution was converged, which corresponded to six units of flow through time ($t = c/U_\infty$). Figure 13 illustrates the aerodynamic forces versus the number of time steps. The forces typically begin with quite high fluctuations and then settle into a constant value as the time step increases further.

1. Aerodynamic Performance

Figure 14a shows the lift coefficients C_L of the Zimmerman and inverse-Zimmerman wings. The lift slopes are near constant for angles of attack $\alpha \leq 9$ deg, and C_L curves become nonlinear as $\alpha \geq 9$ deg. In general, the Zimmerman wing has higher lift than the inverse-Zimmerman wing at all incidences before stall. Both wing planforms have the same stall angle of 12 deg. The upward shift of the lift curve for the Zimmerman wing is due to its higher effective positive camber from the larger local span at around $25\%c$. Figure 14b shows the drag coefficient C_D for both wings, and the Zimmerman wing shows lower values at moderate incidences. As a result, a much better aerodynamic performance is achieved with the Zimmerman wing, as shown in Table 5.

For a thin airfoil, the aerodynamic center is at the one-quarter chord location. The C_{Mac} plot around the one-quarter mean aerodynamic chord is shown in Fig. 14c. Here, the Zimmerman and inverse-Zimmerman wings show an opposite sign in the C_m slope around the design condition. For the Zimmerman wing at the design condition, the C_m slope is positive, indicating longitudinal instability. On the other hand, the inverse-Zimmerman wing has a negative C_m slope at the design condition, showing longitudinal stability.

Figure 15 shows the lift distribution along the span at the design condition. The Zimmerman wing has a lower C_l distribution at $z/b < 0.6$, and the lift increases dramatically near the wingtip location. For the inverse-Zimmerman wing, on the other hand, the lift C_l drops at the tip suddenly. The reason for the lower lift at the wingtip is because the inverse-Zimmerman wing has a maximum span at its maximum reflex camber position (i.e., maximum span at $x/c = 0.85$). The corresponding surface flow pattern in Fig. 16 clearly shows the flow structure for both wing planforms.

2. Stream Pattern

Surface flow visualization of the Zimmerman and inverse-Zimmerman wings at the design condition is given in Fig. 16. Figure 17 shows the spanwise pressure distribution at different chordwise locations. The stream pattern shows that different flow structures form due to different wing planforms. The wing planform affected both the wingtip vortex formation and separation bubble variations on both the upper and lower wing surfaces.

At the design condition, both the Zimmerman and inverse-Zimmerman wings in Fig. 16a show the upper wing separation occurs at $x/c = 0.25$ (maximum positive camber location), and the reattachment is located at $x/c = 0.85$ (maximum reflex camber location). This contrasts with the upper surface flow structures for the

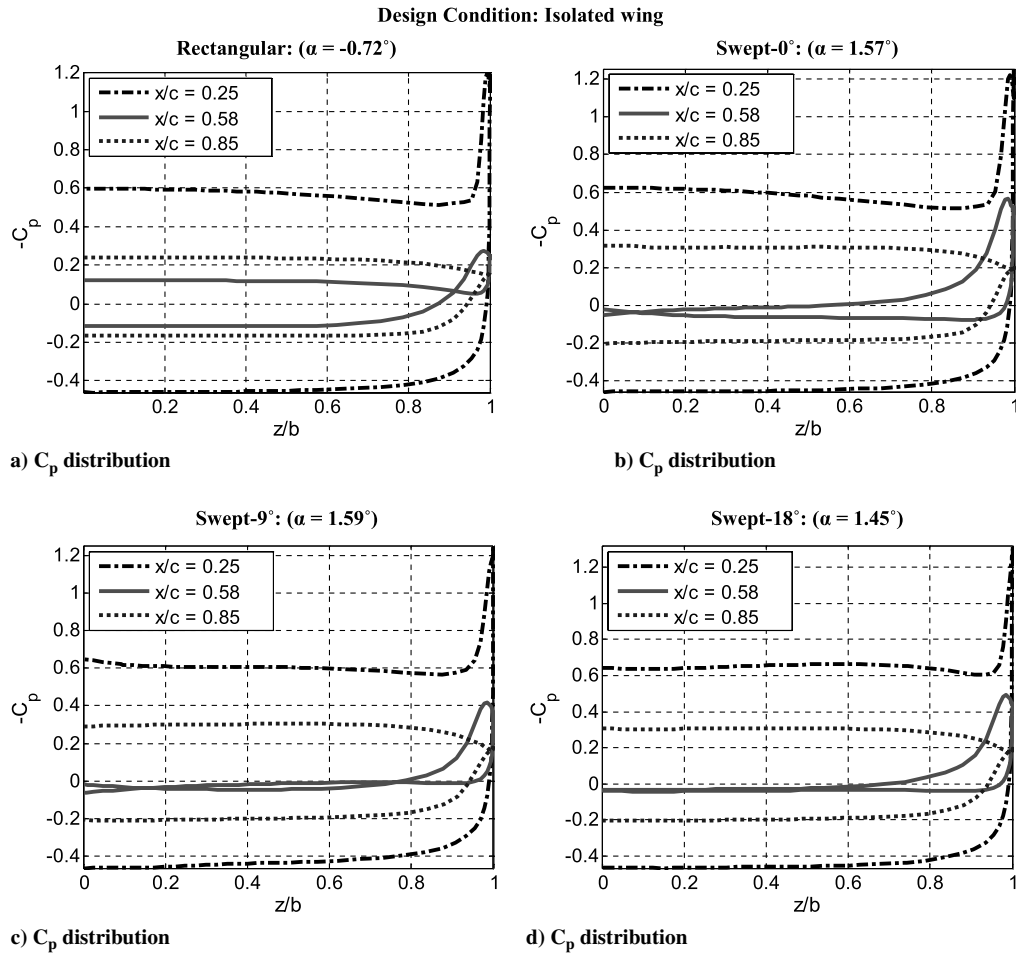


Fig. 12 Spanwise C_p distributions at different chordwise locations at the design condition.

trapezoidal wings discussed in the last section. The confined elliptical shaped separation bubbles on both upper wing surfaces has a similar length in its chordwise direction due to the camber variation, but a shorter size has been found on the Zimmerman wing surface in its spanwise direction. In general, the area occupied by the separation bubbles on the inverse-Zimmerman wing is larger than that for the Zimmerman wing. This leads to the increased drag and therefore poorer aerodynamic performance. The leading-edge vortex, on the other hand, has different structures due to the wing planform effect.

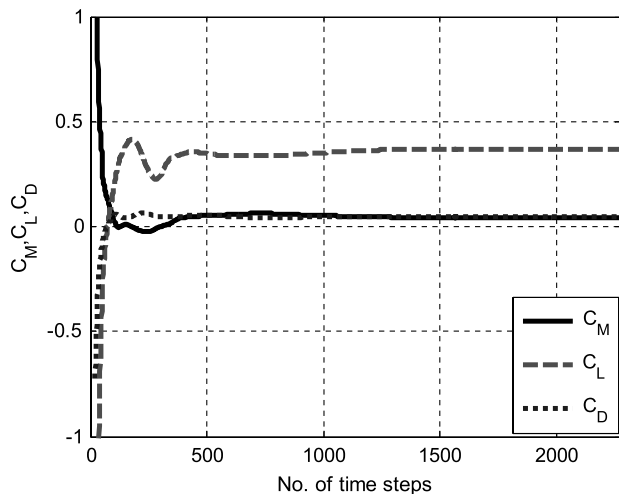


Fig. 13 Aerodynamic force development.

On the inverse-Zimmerman wing, the large leading-edge vortices induce a strong lateral flow toward the edge and generate the secondary vortices, as shown on the surface stream pattern in Fig. 16a. Spanwise flow at the trailing edge has increased due to the reflex camber effect. Although the flow on the upper wing surfaces is separated over a significant area, the lift continues to increase with the incidence. This phenomenon can be attributed to the additional lift from the wingtip vortices, which counteracts the negative effects of flow separation on lift. On the lower wing surfaces, separation bubbles form at both the leading and trailing edges on the inverse-Zimmerman wing. The Zimmerman wing, however, has only the leading-edge bubble on the lower wing surface at the design condition, as shown in Fig. 16b.

To investigate the vortex lift on the wings, the spanwise pressure distributions at different chordwise locations are shown in Fig. 17. Three different streamwise locations are plotted at $x/c = 0.25$ (maximum positive camber location), $x/c = 0.58$ (zero camber location), and $x/c = 0.85$ (maximum reflex camber location). Note that the inverse-Zimmerman wing's maximum span is located at $x/c = 0.85$; however, the Zimmerman wing's maximum span is at $x/c = 0.25$. Figure 17a shows the pressure distribution from these three locations, and Fig. 17b shows the corresponding C_p values. On the inverse-Zimmerman wing, a pressure suction peak region between $z/b = 0.65$ and $z/b = 0.78$ is observed at the location of $x/c = 0.25$ due to the additional lift generated from the strong leading-edge vortex. A vortex suction region is also observable at $x/c = 0.58$, but it disappears at $x/c = 0.85$ as the leading-edge vortex lifts off the surface. For the Zimmerman wing, the vortex lift (suction) is only observable at $x/c = 25\%c$ to a significantly smaller scale. This can be better comprehended by combining with the wingtip vortex structures shown in Fig. 16. At the design condition of

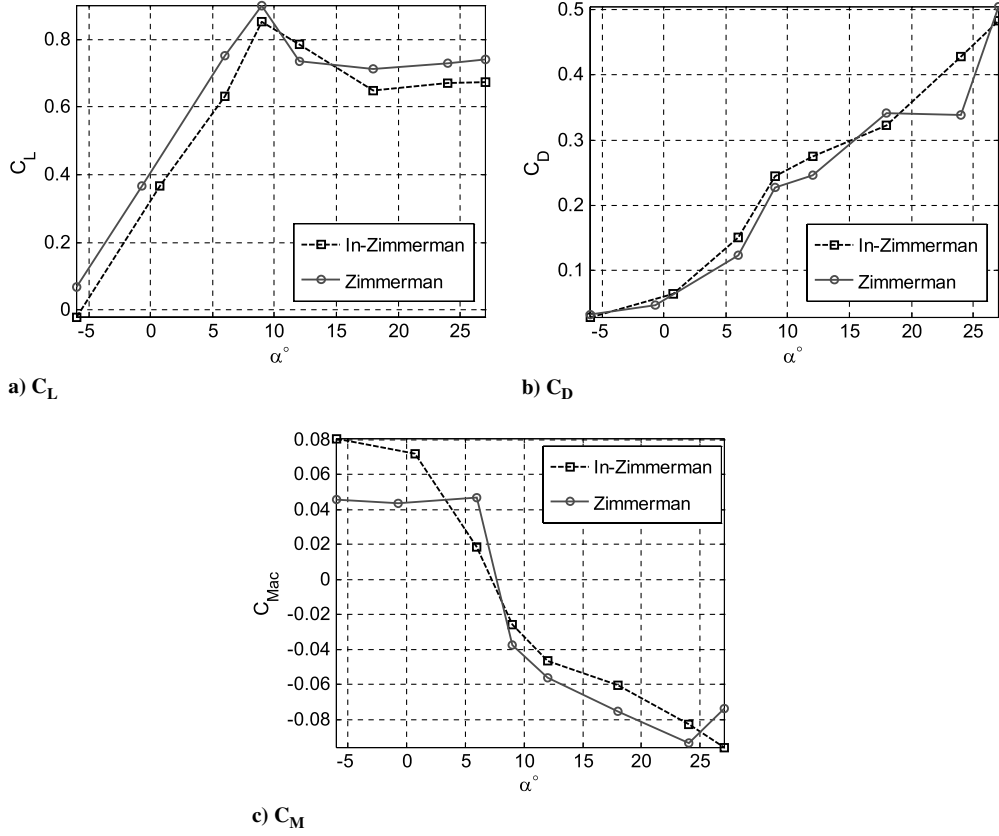


Fig. 14 Aerodynamic coefficients for inverse-Zimmerman and Zimmerman isolated wings: a) C_L , b) C_D , and c) C_M .

the same lift, the inverse-Zimmerman wing benefits from the vortex lift, but the Zimmerman wing benefits more from the positive camber effect.

3. Transition Region

In the solution process, the intermittency factor γ triggers the local transition on the wing surface. The intermittency function turns on the production of the turbulence kinetic energy downstream of the transition point based on the relation between the transition momentum thickness and the strain-rate Reynolds number, which is set to zero in the laminar region and increases to one for fully turbulent flow.

Figures 18 and 19 show the distributions of the intermittency factor γ along the chord at four spanwise locations for the inverse-Zimmerman and Zimmermann wings, respectively. Figures 19 and 20 show the corresponding turbulent kinetic energy contour plots.

The steep increase of the intermittency factor on the upper surface is clearly shown, indicating the transition to turbulent flow. The inverse-Zimmerman planform (Figs. 18 and 20) shows that γ starts to increase approximately at a location of $30\%cat z/b = 0.23$ and reaches a peak

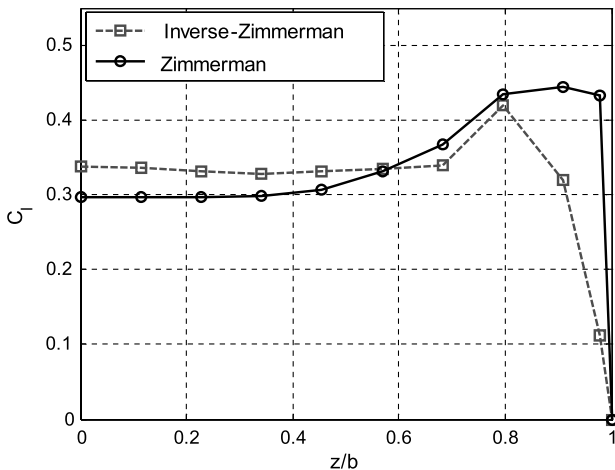


Fig. 15 Spanwise lift distribution at the design condition.

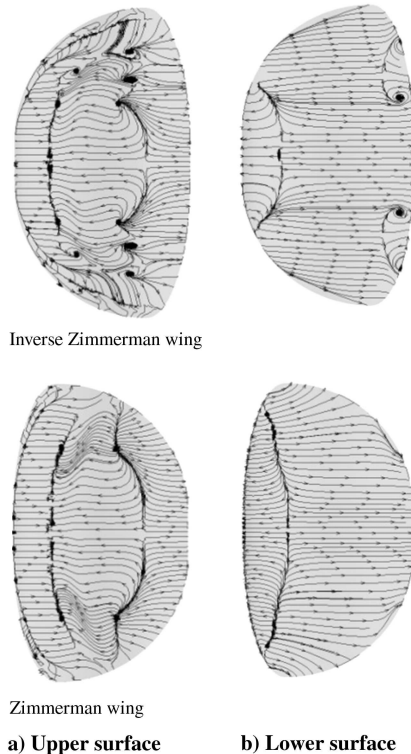


Fig. 16 Instantaneous stream pattern at the design condition ($C_{L=0.35}$): a) upper surface and b) lower surface.

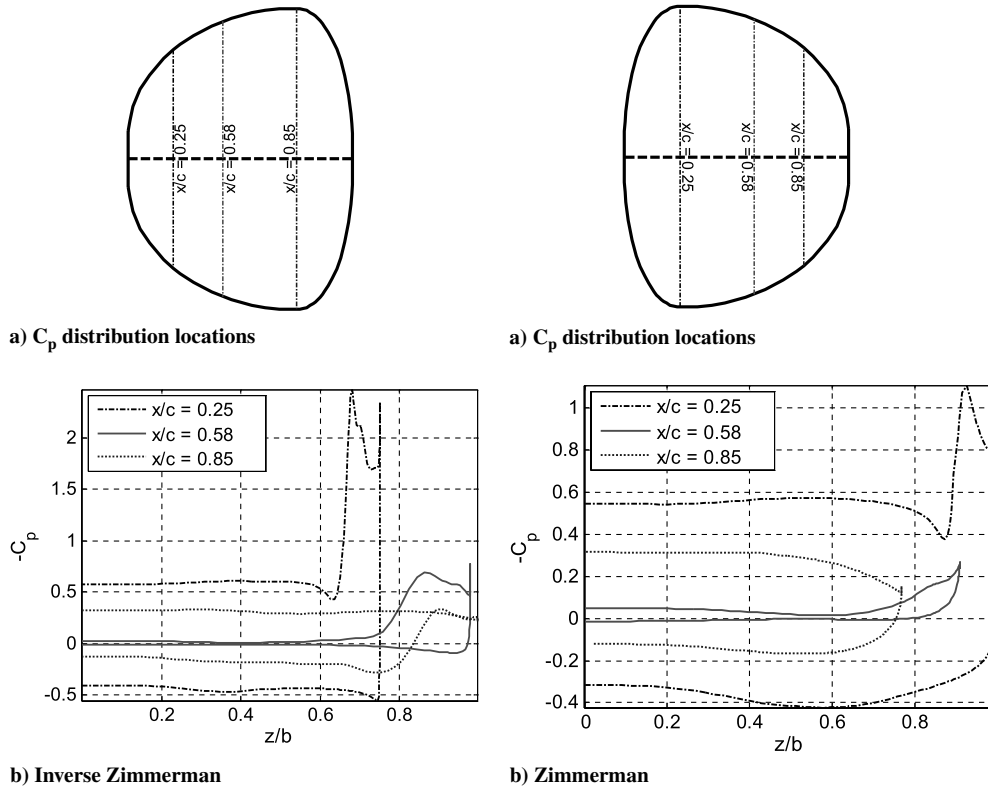


Fig. 17 Mean spanwise C_p distributions at different chordwise locations at the design condition.

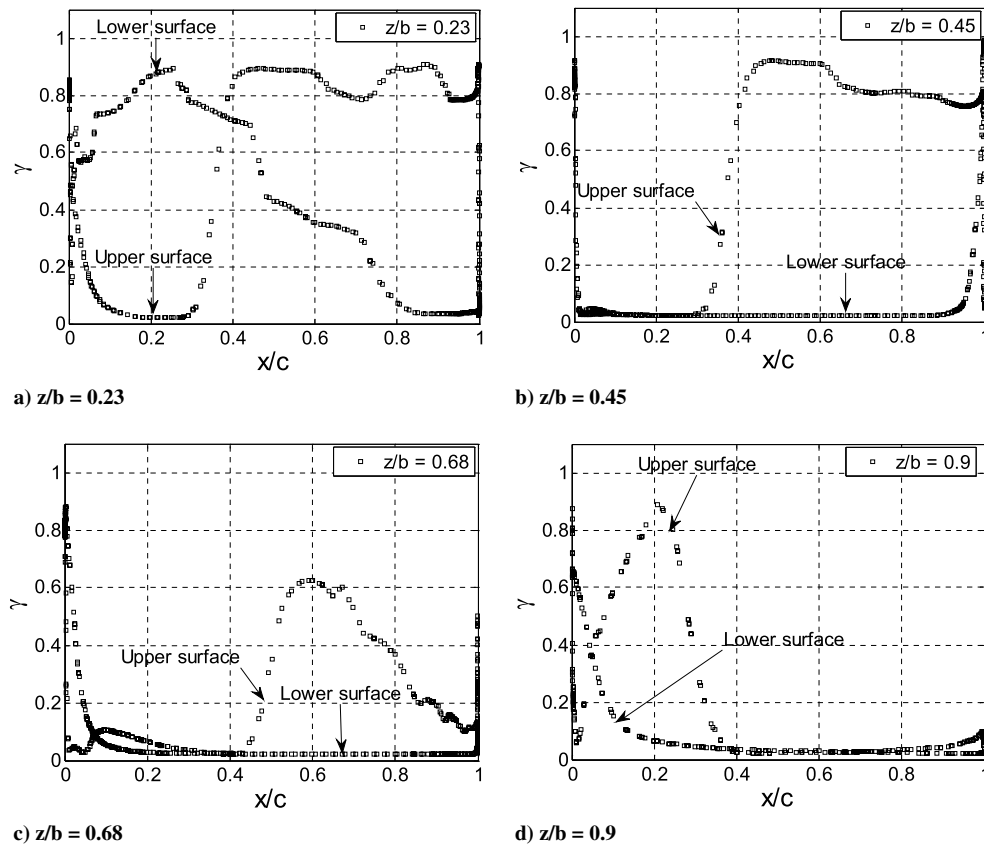


Fig. 18 Instantaneous intermittency values at the design condition for the inverse-Zimmerman wing at a) $z/b = 0.23$, b) $z/b = 0.45$, c) $z/b = 0.68$, and d) $z/b = 0.9$.

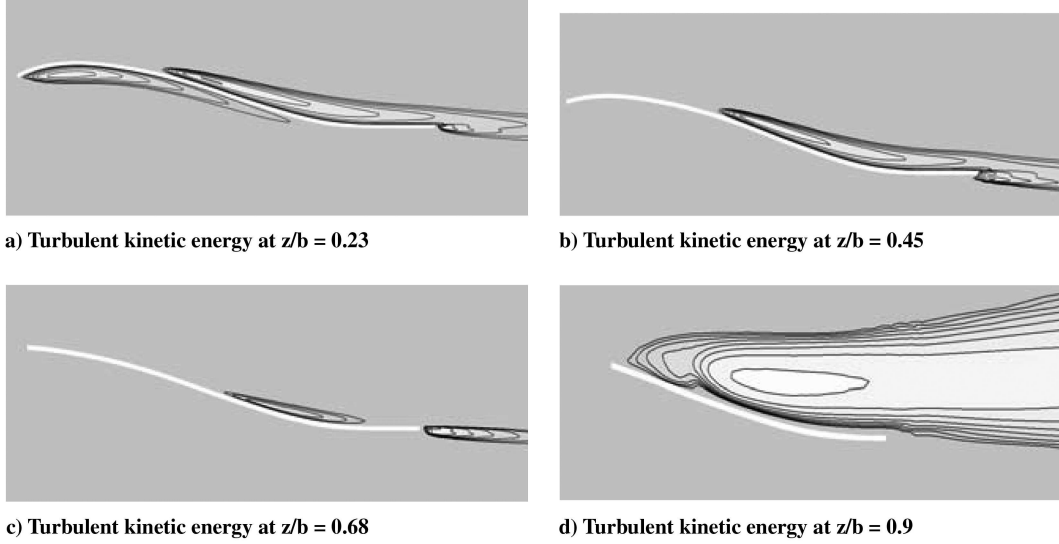


Fig. 19 Turbulent kinetic energy at different span locations for the inverse-Zimmerman wing at a) $z/b = 0.23$, b) $z/b = 0.45$, c) $z/b = 0.68$, and d) $z/b = 0.9$.

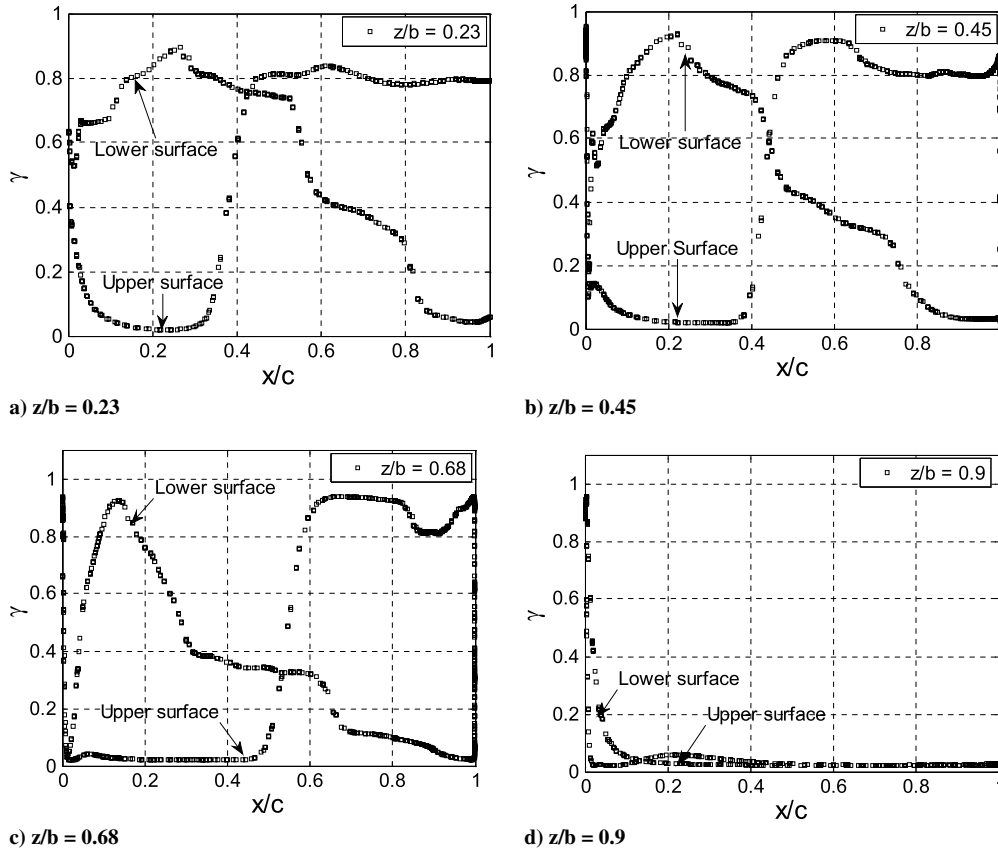


Fig. 20 Instantaneous intermittency values at the design condition for the Zimmerman wing at a) $z/b = 0.23$, b) $z/b = 0.45$, c) $z/b = 0.68$, and d) $z/b = 0.9$.

value of 0.9 at about $40\%c$. Toward the wingtip, the transition location was found at $45\%c$, and a maximum value of 0.6 at about $60\%c$ was shown at the spanwise location of $z/b = 0.68$. At the wingtip, $z/b = 0.9$, vortical flow dominates, and the flow becomes laminar beyond $40\%c$. The lower surface is dominated by laminar flows away from the inboard span region.

The transition region for the Zimmerman wing is shown in Figs. 20 and 21. The transition zone is located approximately between 30 and $40\%c$ at $z/b = 0.23$ on the upper wing surface. The transition region moves toward the trailing edge as the span location moves to the

wingtip (i.e., 46 to $62\%c$ at $z/b = 0.68$). At the wingtip, the flow is dominated by laminar flows. The lower surface shows a much longer transition zone with gradual reduction of the intermittency toward the trailing edge except near the tip.

V. Conclusions

Similar aerodynamic results are observed for trapezoidal wings with different leading-edge sweeps in the low incidence range at a low Reynolds number. However, at higher incidences, the leading-

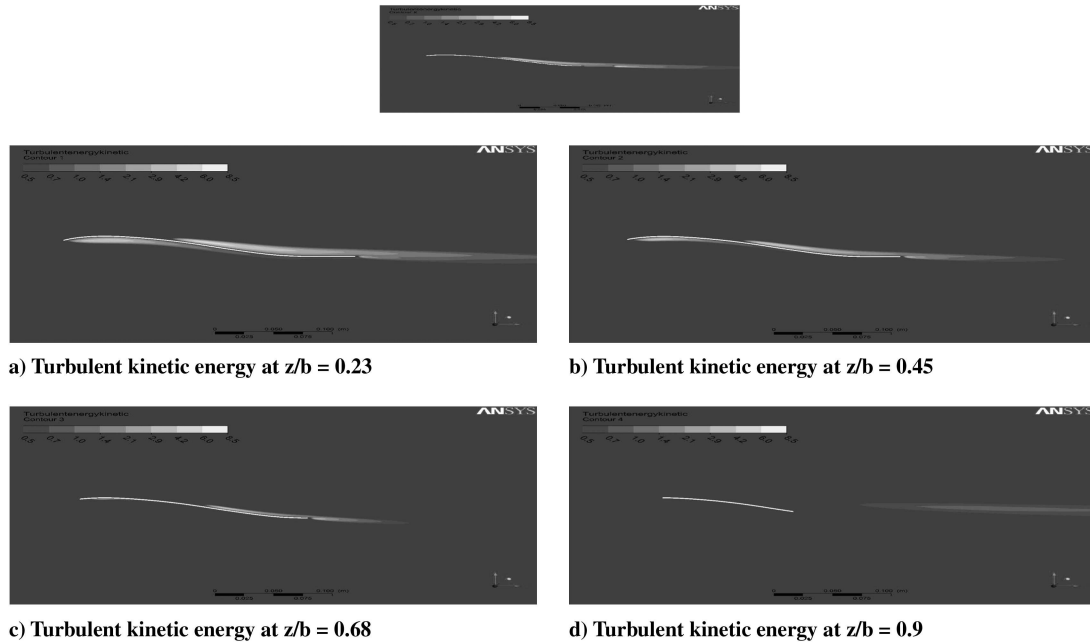


Fig. 21 Instantaneous turbulent kinetic energy values at different span locations for the Zimmerman wing at a) $z/b = 0.23$, b) $z/b = 0.45$, c) $z/b = 0.68$, and d) $z/b = 0.9$.

edge sweep affects directly the stall behavior. Different lift-curve behaviors are found in the near- and poststall conditions for different planforms with positive and reflex cambers. A higher leading-edge sweep gives a higher maximum lift, accompanied by a more sudden stall. On the other hand, a lower leading-edge sweep produces less maximum lift and more gradual stall behavior. All wing planforms except the inverse-Zimmerman wing show a positive pitching moment slope $C_{M\alpha}$ at incidence $\alpha < 5$ deg, which indicates that the micro air vehicle wings themselves are not longitudinally stable at the design condition. The inverse-Zimmerman wing, however, shows longitudinal stability at the design condition, due to the amplified reflex camber by the increased span near the rear of the wing. According to the overall aerodynamic performance, the Zimmerman wing shows the best lift-to-drag ratio, $C_L/C_D = 8$, at the design condition, whereas the trapezoidal wing with a leading-edge sweep above 18 deg produces the highest maximum lift.

The flow visualization on both upper and lower surfaces is used to analyze the different flow structures at the design condition for the different planforms. The observations are the following:

1) Elliptical separation bubbles form on both upper and lower surfaces for the Zimmerman and inverse-Zimmerman wings. They are much larger for the latter. However, for trapezoidal wings, fully attached flow is observed on the upper surface, with separation bubbles forming at the leading-edge region on the lower wing surface.

2) The local camber has a strong effect on the separation/reattachment location of the bubbles for the Zimmerman and inverse-Zimmerman wings. The upper surface separation starts at around $x/c = 0.25$, the maximum positive camber location, and reattaches around $x/c = 0.85$, the maximum reflex camber location for both planforms.

3) The Zimmerman wing shows the wingtip vortex developing from the maximum span location, whereas the inverse-Zimmerman wing has a much earlier start of the wingtip vortices. The vortices generally follow the outline of the wing up to a point and then separate from the wing. The leading-edge vortices affect a much larger area on the inverse-Zimmerman wing upper surface than that on the Zimmerman wing. This helps the inverse-Zimmerman wing to generate more vortex lift. The bubbles on the Zimmerman and inverse-Zimmerman wings are limited to the inboard section of the wing because, near the wingtips, the tip vortices energize the flow, confining the separation bubbles. On the other hand, for the trapezoidal wings, the effects of the wingtip vortices on the flow structure are very limited.

4) For the Zimmerman and the inverse-Zimmerman wings at the given design lift condition, the transition starts at around 30–40% c on the upper surface away from the wingtip after the laminar separation. The transition on the lower wing surface shows relaminarization toward the trailing edge.

Further investigation is warranted in the following areas: wing reflex camber design for longitudinal stability, wing–fuselage aerodynamic interaction and stability, propeller slipstream effects on the flow structure/aerodynamics/stability, and the fluid-structure-interaction effect due to thin wing flexibility on the overall aerodynamic performances.

Acknowledgments

The first author also would like to acknowledge the financial support from the University of Sheffield for his Ph.D. study. The authors wish to thank both William Null and Sergey Shkarayev of University of Arizona for providing the wind-tunnel data.

References

- [1] Pines, D. J., and Bohorquez, F., "Challenges Facing Future Micro-Air-Vehicle Development," *Journal of Aircraft*, Vol. 43, No. 2, 2006, pp. 290–305. doi:10.2514/1.4922
- [2] Gad-el-Hak, M., "Control of Low-Speed Airfoil Aerodynamics," *AIAA Journal*, Vol. 28, No. 9, 1990, pp. 1537–1552. doi:10.2514/3.25250
- [3] Gad-el-Hak, M., "Micro-Air-Vehicles: Can They be Controlled Better?," *Journal of Aircraft*, Vol. 38, No. 3, 2001, pp. 419–429. doi:10.2514/2.2807
- [4] Pelletier, A., and Mueller, T. J., "Low Reynolds Number Aerodynamics of Low-Aspect-Ratio, Thin/Flat/Cambered-Plate Wings," *Journal of Aircraft*, Vol. 37, No. 5, 2000, pp. 825–832. doi:10.2514/2.2676
- [5] Swanson, T., and Isaac, K. M., "Planform and Camber Effects on the Aerodynamics of Low-Reynolds-Number Wings," *Journal of Aircraft*, Vol. 47, No. 2, 2010, pp. 613–621. doi:10.2514/1.45921
- [6] Tezuka, A., Sunada, Y., and Rinoie, K., "Surface Pressure Distributions on 4% Circular Arc Airfoil at Low Reynolds Number," *Journal of Aircraft*, Vol. 45, No. 6, 2008, pp. 2164–2167. doi:10.2514/1.35365
- [7] Reid, M. R., and Kozak, J., "Thin/Cambered/Reflexed Airfoil Development for Micro Air Vehicle Applications at Reynolds Numbers of 60,000 to 100,000," *AIAA Atmospheric Flight Mechanics Conference and Exhibit*, AIAA Paper 2006-6832, Keystone, Colorado, 2006.

- [8] Null, W., and Shkarayev, S., "Effect of Camber on the Aerodynamics of Adaptive-Wing Micro Air Vehicles," *Journal of Aircraft*, Vol. 42, No. 6, 2005, pp. 1537–1542.
doi:10.2514/1.12401
- [9] Torres, G. E., and Mueller, T. J., "Low-Aspect-Ratio Wing Aerodynamics at Low Reynolds Numbers," *AIAA Journal*, Vol. 42, No. 5, 2004, pp. 865–873.
doi:10.2514/1.439
- [10] Okamoto, M., and Azuma, A., "Aerodynamic Characteristics at Low Reynolds Numbers for Wings of Various Planforms," *AIAA Journal*, Vol. 49, No. 6, 2011, pp. 1135–1150.
doi:10.2514/1.J050071
- [11] Zuo, L. X., and Wang, J. J., "Planform and Flexibility on Lift Characteristics for Flow over Low-Aspect Ratio Wings," *Journal of Aerospace Engineering*, Vol. 23, No. 1, 2010.
doi:10.1061/(ASCE)0893-1321(2010)23:1(55)
- [12] Zhang, P. F., Wang, J. J., Liu, Y., and Wu, Z., "Effect of Tapper Ratio on Aerodynamic Performance of Cropped Nonslender Delta Wings," *Journal of Aircraft*, Vol. 46, No. 1, 2009, pp. 320–325.
doi:10.2514/1.32130
- [13] Jian, T., and Ke-Qin, Z., "Numerical and Experimental Study of Flow Structure of Low-Aspect-RatioWing," *Journal of Aircraft*, Vol. 41, No. 5, 2004, pp. 1196–1201.
doi:10.2514/1.5467
- [14] Ol, M. V., and Gharib, M., "Leading-Edge Vortex Structure of Nonslender Delta Wings at Low Reynolds Number," *AIAA Journal*, Vol. 41, No. 1, 2003, pp. 16–26.
doi:10.2514/2.1930
- [15] Wang, J. J., and Zhang, W., "Experimental Investigations on Leading-Edge Vortex Structures for Flow over Non-Slender Delta Wings," *Journal of Experimental Fluid Mechanics*, Vol. 21, No. 2, 2007, pp. 1–7.
doi:10.1088/0256-307X/25/7/060
- [16] Menter, F. R., "Two-Equation Eddy-Viscosity Turbulence Models for Engineering Applications," *AIAA Journal*, Vol. 32, No. 8, 1994.
doi:10.2514/3.12149
- [17] Wilcox, D. C., "Simulation of Transition with a Two-Equation Turbulence Model," *AIAA Journal*, Vol. 32, No. 2, 1994, pp. 247–255.
- [18] Menter, F. R., Langtry, R. B., Likki, S. R., Suzen, Y. B., Huang, P. G., and Volker, S., "A Correction-Based Transition Model Using Local Variables, Part 1: Model Formulation," *Journal of Turbomachinery*, Vol. 128, 2006, pp. 413–422.
doi:10.1115/1.2184352
- [19] Langtry, R. B., and Menter, F. R., "Correlation-Based Transition Modeling for Unstructured Parallelized Computational Fluid Dynamics Codes," *AIAA Journal*, Vol. 47, No. 12, 2009, pp. 2894–2906.
doi:10.2514/1.42362
- [20] Benyahia, A., "Transition Prediction in Transonic Turbine Configurations Using a Correlation-Based Transport Equation Model," *International Journal of Engineering Systems Modelling and Simulation*, Vol. 3, No. 1, 2011, pp. 36–45.
doi:10.1504/IJESMS.2011.038748
- [21] Dornheim, M. A., "Small Drones Mature," *Aviation Week and Space Technology*, Vol. 159, No. 11, 2003, pp. 63–64.
- [22] Cosyn, P., and Vierendeels, J., "Design of Fixed Wing Micro Air Vehicles," *Aeronautical Journal*, 2007, pp. 315–326.
doi:000247557200005
- [23] Kellogg, J., Bovais, C., Foch, R., McFarlane, H., Sullivan, C., Dahlburg, J., Ramamurti, R., Gordon-Spears, D., Hartley, R., Kamgar-Parsi, B., Pipitone, F., Spears, W., Sciambi, A., and Srull, D., "The NRL Micro Tactical Expendable (MITE) AirVehicle," *Aeronautical Journal*, Vol. 106, No. 1062, 2002, pp. 431–441.
- [24] Mueller, T. J., Kellogg, J. C., Ifju, P. G., and Shkarayev, S. V., *Introduction to the Design of Fixed-Wing Micro Air Vehicles*, AIAA, Reston, VA, 2006, pp. 116–117.
- [25] Flake, J., Frischknecht, B., Hansen, S., Knoebel, N., Ostler, J., and Tuley, B., "Development of the Stableyes Unmanned Air Vehicle," *8th International Micro Air Vehicle Competition*, Univ. of Arizona, Tucson, AZ, 2004, pp. 1–10.
- [26] Stanford, B., Sytsma, M., Albertani, R., Viieru, D., Shyy, W., and Ifju, P., "Static Aeroelastic Model Validation of Membrane Micro Air Vehicle Wings," *AIAA Journal*, Vol. 45, No. 12, 2007, pp. 2828–2837.
doi:10.2514/1.30003
- [27] Boller, C., Kuo, C. M., and Qin, N., "Biologically Inspired Shape Changing Aerodynamic Profiles and Their Effect on Flight Performance of Future Aircraft," *Advances in Science and Technology*, Vol. 56, edited by Vincenzini, P., and Casciati, F., Embodying Intelligence in Structures and Integrated Systems, 2008, pp. 534–544.

Queries

1. AU: Figure 8 has been changed to grey scale. Please check and confirm.
2. AU: Please check all the references and their citations.
3. AU: Table 2 was not cited in the text and please check and confirm the insertion of the citation for Table 2 in the text.
4. AU: Please review the revised proof carefully to ensure your corrections have been inserted properly and to your satisfaction.